Chapter 56

Lattice Boltzmann Method for Computational Fluid Dynamics

Li-Shi Luo[1], Manfred Krafczyk[2], and Wei Shyy[3]

[1] *Department of Mathematics & Statistics and Center for Computational Sciences, Old Dominion University, Norfolk, USA*
[2] *Institute for Computational Modeling in Civil Engineering, Technische Universität Braunschweig, Braunschweig, Germany*
[3] *Department of Aerospace Engineering, University of Michigan, Ann Arbor, MI, USA*

1 THEORY OF THE LATTICE BOLTZMANN EQUATION

The lattice Boltzmann equation (LBE) was proposed more than twenty years ago as a successor to the lattice-gas cellular automata (LGCA) as a model for hydrodynamic systems. Both the LGCA and the LBE are based on microscopic and discrete descriptions of fluids, as opposed to macroscopic and continuum descriptions, which are the theoretical foundation of fluid dynamics. In the late two decades, the lattice Boltzmann (LB) method has advanced to such an extent that it has become a versatile and competitive alternative for computational fluid dynamics (CFD) in several areas. In this short survey on the current status of the LB method, we will provide a concise introduction to the theoretical underpinning of the LBE and discuss the areas in which the LB method has been proven to be useful and successful. This survey is not intended to be a comprehensive review. Historic reviews on the early development of the LGCA and LBE can be found in Rothman and Zaleski (1997) and Chen and Doolen (1998).

Encyclopedia of Aerospace Engineering.
Edited by Richard Blockley and Wei Shyy
© 2010 John Wiley & Sons, Ltd. ISBN: 978-0-470-75440-5

1.1 Mathematical background

We will first discuss the theoretical underpinning of the LBE. The LBE method differentiates itself from all conventional methods for CFD based on direct discretizations of the Navier–Stokes equations because it is derived from the linearized Boltzmann equation (He and Luo, 1997):

$$\partial_t f + \boldsymbol{\xi} \cdot \nabla f = \frac{1}{\epsilon} \mathcal{L}\left[f - f^{(0)}\right],$$
$$f^{(0)} = \rho(2\pi RT)^{-3/2} e^{-c^2/2RT} \tag{1}$$

where $f := f(\boldsymbol{x}, \boldsymbol{\xi}, t)$ is the single particle distribution function in phase space $\Gamma := (\boldsymbol{x}, \boldsymbol{\xi})$; $\boldsymbol{\xi} := \dot{\boldsymbol{x}}$ is the *particle* velocity; $\mathcal{L}$ is the linearized collision operator; $\epsilon := Kn := \ell/L$ is the Knudsen number, which is the ratio of the molecular mean-free path ℓ and a macroscopic characteristic length L, $f^{(0)} = f^{(0)}(\rho, \boldsymbol{u}, T)$ is the Maxwell equilibrium distribution; R is the gas constant; $\boldsymbol{c} := (\boldsymbol{\xi} - \boldsymbol{u})$ is the peculiar velocity; and ρ, $\boldsymbol{u}$, and T are the mass density, velocity, and temperature of

the flow, respectively, which are moments of f with respect to $\boldsymbol{\xi}$:

$$\begin{pmatrix} \rho \\ \rho \boldsymbol{u} \\ \rho(u^2 + 3RT) \end{pmatrix} = \int f \begin{pmatrix} 1 \\ \boldsymbol{\xi} \\ \xi^2 \end{pmatrix} \mathrm{d}\boldsymbol{\xi} = \int f^{(0)} \begin{pmatrix} 1 \\ \boldsymbol{\xi} \\ \xi^2 \end{pmatrix} \mathrm{d}\boldsymbol{\xi} \tag{2}$$

The microscopic conservation laws are encoded in the collision because 1, $\boldsymbol{\xi}$, and $\xi^2 := \boldsymbol{\xi} \cdot \boldsymbol{\xi}$ are collisional invariants, that is,

$$\int \begin{pmatrix} 1 \\ \boldsymbol{\xi} \\ \xi^2 \end{pmatrix} \mathcal{L} \, \mathrm{d}\boldsymbol{\xi} = \begin{pmatrix} 0 \\ \mathbf{0} \\ 0 \end{pmatrix} \tag{3}$$

In the Chapman–Enskog analysis, f is expanded as an asymptotic series of ϵ,

$$f = f^{(0)} + \epsilon f^{(1)} + \cdots + \epsilon^n f^{(n)} + \cdots \tag{4}$$

With $f = f^{(0)}$, the Euler equations are derived from the Boltzmann equation, and with $f = f^{(0)} + f^{(1)}$, the Navier–Stokes equations are derived. The Boltzmann equation is a bridge connecting the macroscopic physics to underlying microscopic dynamics, and the Chapman–Enskog analysis directly relates transport coefficients to molecular interactions.

Numerically solving kinetic equations in phase space $\Gamma := (\boldsymbol{x}, \boldsymbol{\xi})$ and time t is far more challenging computationally than solving hydrodynamic equations in physical space $\boldsymbol{x}$ and t. To construct effective and efficient kinetic schemes for hydrodynamic problems, some judicious approximations must be made. There are three steps to construct the LBE (d'Humières, 1992; d'Humières *et al.*, 2002; Lallemand and Luo, 2000, 2003). The first step is to use a linear relaxation model with a finite number of constant relaxation times to approximate the collision process. That is, the Gross–Jackson procedure is used to reduce the complexity of the collision operator. The second step is to approximate the velocity space $\boldsymbol{\xi}$ with a finite set of q discrete velocities $\mathbb{V} := \{\boldsymbol{c}_i | i = 0, 1, \ldots, b\}$ with $\boldsymbol{c}_0 = \mathbf{0}$ and $q = (1 + b)$, which is usually symmetric, that is, $\mathbb{V} = -\mathbb{V}$. The discrete velocity set $\{\boldsymbol{c}_i\}$ must preserve the hydrodynamic moments of f as well as their fluxes *exactly* (He and Luo, 1997). And the third and final step is to discretize space $\boldsymbol{x}$ and time t *coherently* with the discretization of $\boldsymbol{\xi}$. The space $\boldsymbol{x}$ is discretized into a lattice space $\delta_x \mathbb{Z}_d$ in d dimensions with a lattice constant δ_x and the time t is discretized with a constant time step size δ_t, that is, $t_n \in \delta_t \mathbb{N}_0$, where $\mathbb{N}_0 = \{0, 1, \ldots\}$. The phase space $\Gamma := (\boldsymbol{x}, \boldsymbol{\xi})$ and time t is *coherently* discretized so that for any $\boldsymbol{c}_i \in \mathbb{V}$, the vector $\boldsymbol{c}_i \delta_t$ can always connect one lattice point to another nearby lattice point, that is,

$$\boldsymbol{x}_j + \delta_t \boldsymbol{c}_i \in \delta_x \mathbb{Z}_d, \quad \forall \, \boldsymbol{x}_j \in \delta_x \mathbb{Z}_d \text{ and } \forall \, \boldsymbol{c}_i \in \mathbb{V} \tag{5}$$

The lattice Boltzmann equation with q discrete velocities in d dimensions is denoted as the DdQq model, and it can be concisely written as

$$\mathbf{f}(\boldsymbol{x}_j + \boldsymbol{c}\delta_t, \, t_n + \delta_t) - \boldsymbol{f}(\boldsymbol{x}_j, \, t_n) = -\mathsf{M}^{-1} \cdot \mathsf{S} \cdot \left[\mathbf{m} - \mathbf{m}^{(\mathrm{eq})}\right], \tag{6}$$

where symbols in bold-face font denote q-dimensional column vectors,

$$\begin{aligned} &\mathbf{f}(\boldsymbol{x}_j + \boldsymbol{c}\delta_t, \, t_n + \delta_t) := (f_0(\boldsymbol{x}_j, \, t_n + \delta_t), \\ &\quad f_1(\boldsymbol{x}_j + \boldsymbol{c}_1\delta_t, \, t_n + \delta_t), \ldots, \, f_b(\boldsymbol{x}_j + \boldsymbol{c}_b\delta_t, \, t_n + \delta_t))^\dagger, \\ &\mathbf{f}(\boldsymbol{x}_j, \, t_n) := (f_0(\boldsymbol{x}_j, \, t_n), \, f_1(\boldsymbol{x}_j, \, t_n), \ldots, \, f_b(\boldsymbol{x}_j, \, t_n))^\dagger, \\ &\mathbf{m}(\boldsymbol{x}_j, \, t_n) := (m_0(\boldsymbol{x}_j, \, t_n), \, m_1(\boldsymbol{x}_j, \, t_n), \ldots, \, m_b(\boldsymbol{x}_j, \, t_n))^\dagger, \\ &\mathbf{m}^{(\mathrm{eq})}(\boldsymbol{x}_j, \, t_n) := (m_0^{(\mathrm{eq})}(\boldsymbol{x}_j, \, t_n), \\ &\quad m_1^{(\mathrm{eq})}(\boldsymbol{x}_j, \, t_n), \ldots, \, m_b^{(\mathrm{eq})}(\boldsymbol{x}_j, \, t_n))^\dagger \end{aligned} \tag{7}$$

where "†" denotes transpose, $q = (1 + b)$, M is a $q \times q$ matrix that maps a vector $\mathbf{f}$ in the velocity space $\mathbb{V} = \mathbb{R}^q$ to a vector m in the moment space $\mathbb{M} = \mathbb{R}^q$,

$$\mathbf{m} = \mathsf{M} \cdot \mathbf{f}, \quad \mathbf{f} = \mathsf{M}^{-1} \cdot \mathbf{m} \tag{8}$$

and S is a $q \times q$ diagonal matrix of relaxation rates $\{s_i\}$, $s_i \in (0, \, 2) \; \forall i$,

$$\mathsf{S} = \mathrm{diag}(s_0, \, s_1, \, \ldots, \, s_b) \tag{9}$$

The relaxation rates $\{s_i\}$ determine the transport coefficients in the system. The components of $m^{(\mathrm{eq})}$ are the equilibrium moments, which are polynomials of the conserved moments of the system. For athermal hydrodynamics $RT = (1/3)c^2$, where $c := \delta_x/\delta_t$, and $\mathbf{m}^{(\mathrm{eq})}$ is of first order in ρ, the density, and second-order in $\boldsymbol{u}$, the flow velocity. A forcing term $\boldsymbol{F}$ can be included in the LBE using the following formula (Luo, 2000; Lallemand and Luo, 2003),

$$f_i^* = f_i - \frac{2w_i}{c_s^2} \boldsymbol{c}_i \cdot \boldsymbol{F} \tag{10}$$

where coefficients $\{w_i\}$ are determined by $\{\boldsymbol{c}_i\}$, and c_s is the speed of sound in the system and $c_s = (1/\sqrt{3})c$.

With a given discrete velocity set $\{\boldsymbol{c}_i\}$, the matrix M can be easily constructed (Lallemand and Luo, 2000, 2003; d'Humières *et al.*, 2002). We can also derive the LB models for multi-phase nonideal gases (Luo, 2000) and multi-component mixtures (Asinari and Luo, 2008).

The lattice Boltzmann equation (6) is a projection method: The collision is executed in the moment space $\mathbb{M}$ spanned by an orthogonal basis, while the advection is carried out in the velocity space $\mathbb{V}$. The LBE (6) can be decomposed into two independent steps:

$$\text{Collision:}\quad \mathbf{f}^*(\boldsymbol{x}_j,\, t_n) = \mathbf{f}(\boldsymbol{x}_j,\, t_n) - \mathsf{M}^{-1}\cdot\mathsf{S} \cdot \left[\mathbf{m}(\boldsymbol{x}_j,\, t_n) - \mathbf{m}^{(\mathrm{eq})}(\boldsymbol{x}_j,\, t_n)\right], \tag{11a}$$

$$\text{Advection:}\quad \mathbf{f}(\boldsymbol{x}_j + \boldsymbol{c}\delta_t,\, t_n + \delta_t) = \mathbf{f}^*(\boldsymbol{x}_j,\, t_n). \tag{11b}$$

where $\mathbf{f}$ and $\mathbf{f}^*$ denote pre-collision and post-collision distributions, respectively. The collision is completely *local*, while the advection moves data from one grid point to another with no floating number operations, but it does consume CPU time for data communications.

The lattice Boltzmann algorithm defined by equation (6) can be viewed as an explicit finite difference scheme on a uniform Cartesian mesh and with stencils defined by the discrete velocities $\{\boldsymbol{c}_i\}$. The LB method described above is restricted to near incompressible flows without shocks. However, the LB method is also inherently compressible in the sense that density fluctuations are an intrinsic part of the LBE, similar to the artificial compressibility method. It can be shown that the LBE method is second-order accurate in space and first-order accurate in time for the incompressible Navier–Stokes equation (Junk, Klar and Luo, 2005). The LBE has relatively low numerical dissipation and dispersion and better isotropy compared to other conventional second- or even higher-order methods (Lallemand and Luo, 2000; Maríe, Ricot and Sagaut, 2009).

1.2 Large eddy simulation

Because the strain rates $\sigma_{\alpha\beta} := (\partial_\alpha u_\beta + \partial_\beta u_\alpha)/2$ are related to the second-order moments of f_i and they are readily available in the LBE (Krafczyk, Tölke and Luo, 2003; Yu, Luo and Girimaji, 2006), the Smagorinsky subgrid model can be easily implemented,

$$\nu = \nu_0 + \nu_\mathrm{t} = c_s^2\left(\frac{1}{s_\nu} - \frac{1}{2}\right), \quad \nu_\mathrm{t} = (C_S\delta_x)^2\,\bar{S},$$
$$\bar{S} = \sqrt{2\Sigma_{\alpha,\beta}\sigma_{\alpha\beta}\sigma_{\alpha\beta}} \tag{12}$$

where ν_0 and ν_t are molecular and turbulent viscosities, respectively. For a flow with the Reynolds number $Re = UL/\nu_0$, the relaxation rate s_ν for the stresses is determined by

$$\frac{1}{s_\nu} = \frac{1}{c_s^2}\left(\frac{UL}{Re} + \nu_\mathrm{t}\right) + \frac{1}{2} \tag{13}$$

1.3 Boundary conditions

The no-slip boundary conditions in the LBE can be easily realized by using the bounce-back (BB) boundary conditions (BCs): A "particle" f_i reverses its momentum $\boldsymbol{c}_i$ after colliding with a no-slip wall, that is,

$$f_{\bar{i}}^*(\boldsymbol{x}_\mathrm{b},\, t_n) = f_i(\boldsymbol{x}_\mathrm{b},\, t_n) - \frac{2w_i\rho_\mathrm{b}\boldsymbol{u}_\mathrm{w}\cdot\boldsymbol{c}_i}{c_s^2} \tag{14}$$

where $f_{\bar{i}}^*$ the post-collision distribution function corresponding to $\boldsymbol{c}_{\bar{i}} := -\boldsymbol{c}_i$; $\boldsymbol{x}_\mathrm{b}$ is a fluid node adjacent to a boundary; $\boldsymbol{u}_\mathrm{w}$ is the velocity imposed at the boundary point where particle-boundary collision occurs; and $\rho_\mathrm{b} = \rho(\boldsymbol{x}_\mathrm{b})$. The bounce-back boundary conditions can also be used to realize pressure conditions at a boundary location $\boldsymbol{x}_\mathrm{w}$ by using $\rho_\mathrm{b} = \rho(\boldsymbol{x}_\mathrm{w}) = p(\boldsymbol{x}_\mathrm{w})/c_s^2$, where $p(\boldsymbol{x}_\mathrm{w})$ is the imposed pressure.

The bounce-back boundary conditions approximate a smooth curved boundary with zig-zag staircases. Interpolations can be used to improve geometric accuracy (Bouzidi, Firdaouss and Lallemand, 2001). Because Dirichlet boundary conditions are satisfied at the location that depends on two relaxation rates (Ginzburg and d'Humières, 2003), it is imperative to use the MRT-LBE model in order to achieve accurate boundary conditions in the LBE.

1.4 Fluid–fluid and fluid–surface interactions

Diffusive interface methods are often used in the LBE to capture an interface between two immiscible fluids (e.g., oil–water) or fluids of two different phases (e.g., vapor–water). We introduce the order parameter

$$\phi := \frac{\rho_\mathrm{A} - \rho_\mathrm{B}}{\rho_\mathrm{A} + \rho_\mathrm{B}} \tag{15}$$

where ρ_A and ρ_B are the densities for two components or phases in a mixture, respectively. A vector related the gradient

of ϕ is computed as the following:

$$\boldsymbol{C}(\boldsymbol{x}_j) = \frac{1}{c_s^2\delta_t}\sum_i w_i \boldsymbol{c}_i \phi(\boldsymbol{x}_j + \boldsymbol{c}_i\delta_t) \approx \frac{1}{c_s^2\delta_t}\sum_i w_i \boldsymbol{c}_i\boldsymbol{c}_i \cdot \nabla\phi(\boldsymbol{x}_j) \quad (16)$$

The surface tension is related to $\boldsymbol{C}$ and can be directly included in the equilibria of the stresses. An anti-diffusion algorithm, which maximizes $\rho_{\mathrm{A}}\boldsymbol{u}_{\mathrm{A}} \cdot \boldsymbol{C}$, is used to separate two species ρ_{A} and ρ_{B}, and hence to sharpen fluid-fluid interfaces (Tölke *et al.*, 2002; Tölke, Freudiger and Krafczyk, 2006).

To model a solid surface with different wettability, we can "coat" the surface with the order parameter $\phi_{\mathrm{w}} \in [-1,\ +1]$. For instance, if a surface is characterized with $\phi_{\mathrm{w}} = +1$, then it is hydrophilic to species "A" and hydrophobic to species "B." With properties of surface and both species given, the contact angle can be determined analytically.

2 APPLICATIONS IN COMPUTATIONAL FLUID DYNAMICS

In what follows, we will show a few selected examples to demonstrate the capability of the LB method. These examples include direct numerical simulations (DNS) of incompressible decaying homogeneous isotropic turbulence, large eddy simulations (LES) of the flow past a smooth sphere, particulate suspensions in fluid, a droplet sliding on an inclined surface under gravity, and multi-component flows through porous media.

2.1 DNS of incompressible decaying turbulence

The incompressible decaying homogeneous isotropic turbulence (DHIT) is the solution of the incompressible Navier–Stokes equation in a 3D cube with periodic boundary conditions:

$$\partial_t\boldsymbol{u} + \boldsymbol{u}\cdot\nabla\boldsymbol{u} = -\nabla p + \nu\nabla^2\boldsymbol{u}, \quad \nabla\cdot\boldsymbol{u} = 0, \quad \boldsymbol{x} \in [0,\ 2\pi]^3,\ t \geq 0 \quad (17)$$

where p is the pressure and ν is the shear viscosity; and $\boldsymbol{u}(\boldsymbol{x} + 2\pi\boldsymbol{L},\ t) = \boldsymbol{u}(\boldsymbol{x},\ t)$, $\boldsymbol{L} := (m,\ n,\ l)$, for any arbitrary integers m, n, and l. The initial velocity field $\boldsymbol{u}_0(\boldsymbol{x})$ is randomly generated with a zero-mean Gaussian distribution and satisfies the following initial energy spectrum:

$$E_0(k) := E(k,\ t=0) = Ak^4 e^{-0.14k^2}, \quad k \in [k_a,\ k_b] \quad (18)$$

where $A = 1.4293 \times 10^{-4}$, $k_a = 3$, and $k_b = 8$. The DHIT is characterized by its root-mean-square (RMS) velocity $u' := \sqrt{\langle \boldsymbol{u}\cdot\boldsymbol{u}\rangle/3}$ and the Taylor micro-scale Reynolds number,

$$Re_\lambda = \frac{u'\lambda}{\nu}, \quad \lambda = \sqrt{\frac{15\nu}{\varepsilon}}u' \quad (19)$$

where ε is the dissipation rate. The statistical quantities relevant to DHIT include the energy K, the dissipation rate ε, the energy spectrum $E(\boldsymbol{k},\ t)$, the skewness S_u, and the flatness F_u,

$$K = \frac{1}{2}\langle \boldsymbol{u}\cdot\boldsymbol{u}\rangle, \quad \varepsilon = 2\nu\langle \boldsymbol{u}\cdot\nabla^2\boldsymbol{u}\rangle,$$
$$E(\boldsymbol{k},\ t) = \frac{1}{2}\tilde{\boldsymbol{u}}(\boldsymbol{k},\ t)\cdot\tilde{\boldsymbol{u}}(\boldsymbol{k},\ t) \quad (20)$$
$$S_u = \frac{1}{3}\sum_{\alpha=1}^{3} S_\alpha, \quad S_\alpha = \frac{\left\langle(\partial_\alpha u_\alpha)^3\right\rangle}{\left\langle(\partial_\alpha u_\alpha)^2\right\rangle^{3/2}},$$
$$F_u = \frac{1}{3}\sum_{\alpha=1}^{3} F_\alpha, \quad F_\alpha = \frac{\left\langle(\partial_\alpha u_\alpha)^4\right\rangle}{\left\langle(\partial_\alpha u_\alpha)^2\right\rangle^2} \quad (21)$$

Due to the simplicity of the boundary conditions in DHIT, pseudo-spectral (PS) methods are the *de facto* method for this problem. We use the D3Q19 LBE model and compare a pseudo-spectral (PS) method with a second-order Adam-Bashforth scheme for time integration (Peng *et al.*, 2009). The mesh size is $N^3 = 128^3$ and $Re_\lambda = 24.37$. The simulations are carried out to $t' = t/\tau_0 \approx 30$, where $\tau_0 = K_0/\varepsilon_0$ is the turbulence turnover time. Both the LBE and PS methods use the same dimensionless time step size $\delta t' = \delta t/\tau_0$.

The normalized kinetic energy $K(t')/K(0)$, the normalized dissipation rate $\varepsilon(t')/\varepsilon(0)$, the energy spectra $E(k,\ t')$, the skewness $S_u(t')$, and the flatness $F_u(t')$ are shown in Figure 1. We observe that all these statistical quantities obtained by the LB method agree very well with those obtained by the pseudo-spectral method (Peng *et al.*, 2009).

Figure 2 shows the instantaneous velocity and vorticity fields obtained by the LBE and the pseudo-spectral method. It is remarkable that the flow fields obtained by using these two vastly different methods agree so well with each other (Peng *et al.*, 2009).

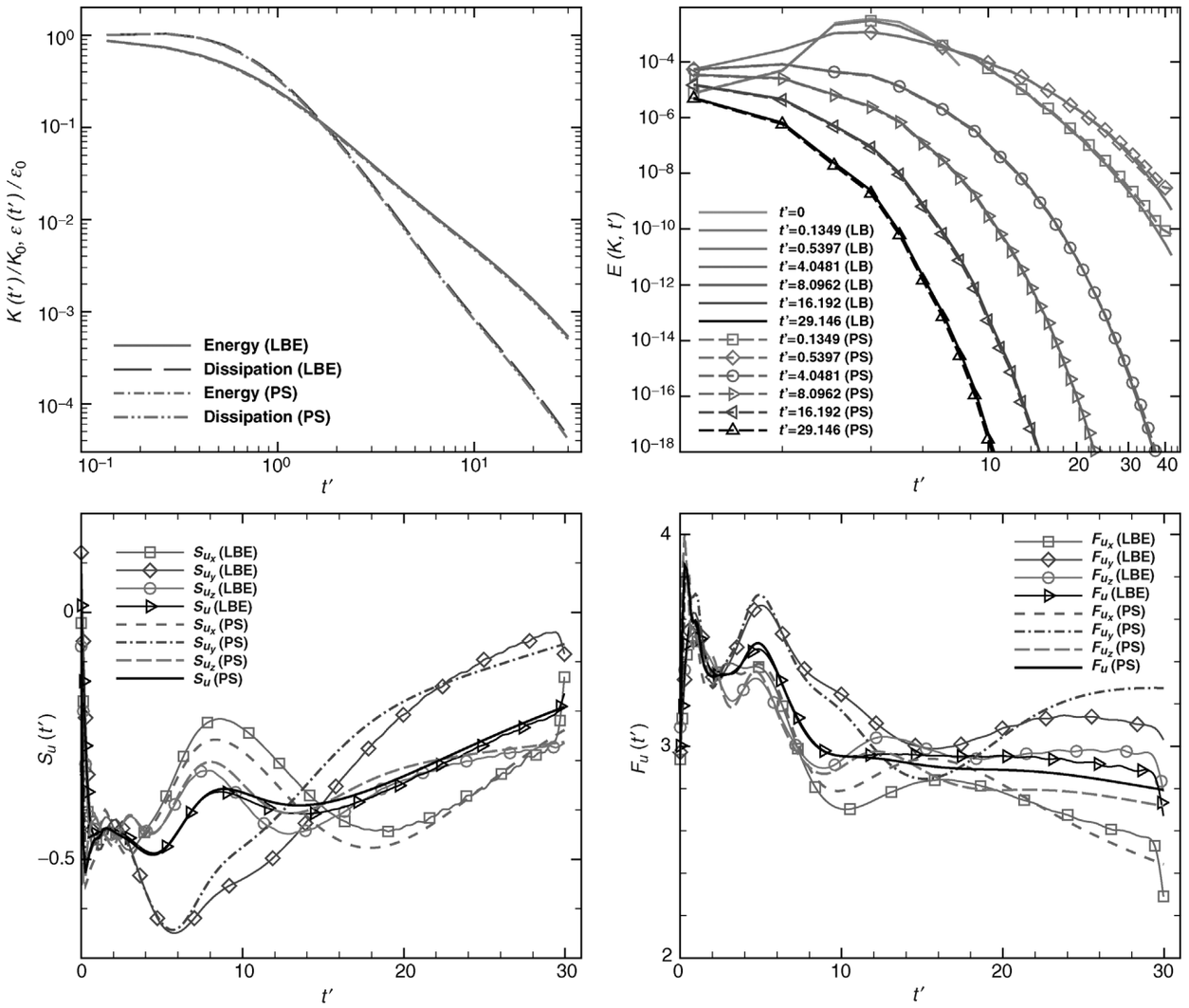

Figure 1. DNS of incompressible DHIT. $N^3 = 128^8$ and $Re_\lambda = 24.37$. (a) $K(t')/K_0$ and $\varepsilon(t')/\varepsilon_0$ (left); the energy spectra $E(k,\ t')$ (right). (b) $S_u(t')$ (left) and $F_u(t')$ (right).

2.2 LES of flow past a smooth sphere

We use the D3Q19 MRT-LBE with the Smagorinsky model to simulate the flow past a sphere in subcritical (laminar separation) conditions with $1000 \leq Re \leq 10\,000$. The domain size is $L \times W \times H = 18D \times 11D \times 11D$, where D is the diameter of the sphere. Slip boundary conditions are applied in four boundaries parallel to the streamwise direction x. A uniform flow is imposed in the inlet, and the fully developed conditions are imposed at the outlet in x direction. The sphere is centered at the yz plane $4.5D$ away from the inlet. We use a multi-block mesh with six-level binary grid-refinements, which has about 2×10^7 grid points. The Mach number is fixed at $M = 0.02$, and $C_S = 0.18$.

Figure 3 shows an iso-surface of u_x in 3D and the vorticity magnitude $\|\boldsymbol{\omega}\|$ at the symmetric xy plane with $Re = 10\,000$. In the LB-LES, the angle of separation is $\theta_s \approx 84^\circ$, compared to $\theta_s = 82.5^\circ$, measured experimentally by Achenbach (1972) and $\theta_s = 84^\circ \pm 1^\circ$, the DES result of Constantinescu and Squires (2002).

In Figure 4 we show the angular distribution of the mean pressure coefficient $\bar{C}_p(\theta)$ with $Re = 10\,000$ and the drag coefficient $C_D(Re)$ as a function of Re with $1000 \leq Re \leq 10\,000$. For $\bar{C}_p(\theta)$, we compare the LB results with the experimental data of Achenbach (1972) and the DES data of Constantinescu and Squires (2002). As for $C_D(Re)$, we compare the LB results with the experimental data of Goin and Lawrence (1968) and the following formula given by Clift, Grace and Weber (1978),

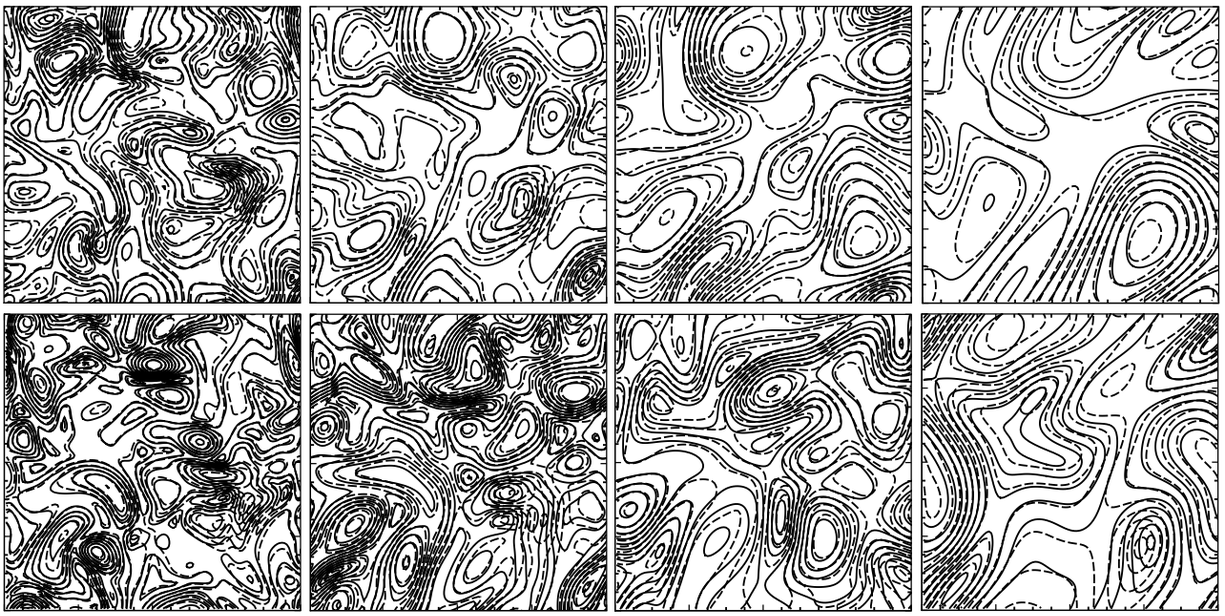

Figure 2. DNS of DHIT. The magnitudes of the velocity $\|\boldsymbol{u}(\boldsymbol{x}, t')/u'\|$ (top row) and the vorticity $\|\boldsymbol{\omega}(\boldsymbol{x}, t')/u'\|$ (bottom row) on the xy plane $z = \pi$. The LBE (solid lines) vs. the pseudo-spectral method (dashed lines). From left to right: $t' = 4.048\,169$, 8.095 571, 16.18 959, and 29.94 941.

$$C_D \approx \mathrm{e}^{-5.657681832+2.5558x-0.04036767209x^2+0.01978536702x^3},$$
$$x := \ln Re \tag{22}$$

For both $\bar{C}_p(\theta)$ and $C_D(Re)$, the LBE–LES results agree well with existing data.

2.3 Particulate suspensions

With the bounce-back boundary conditions, the net momentum change due a particle-boundary collision is $-2w_i\rho\boldsymbol{u}_\mathrm{w}\cdot\boldsymbol{c}_i$ along the direction of $\boldsymbol{c}_i$. Consequently, the total force $\boldsymbol{F}$ and torque $\boldsymbol{T}$ on a particle are

$$\boldsymbol{F} = -\sum_{\substack{\boldsymbol{c}_i\in\mathbb{B}\\ \boldsymbol{x}_k\in\partial\Omega}} 2w_i\rho\,\boldsymbol{u}_\mathrm{w}\cdot\boldsymbol{c}_i\,\hat{\boldsymbol{c}}_i,$$
$$\boldsymbol{T} = \sum_{\substack{\boldsymbol{c}_i\in\mathbb{B}\\ \boldsymbol{x}_k\in\partial\Omega}} 2w_i\rho\,\boldsymbol{u}_\mathrm{w}\cdot\boldsymbol{c}_i\,\hat{\boldsymbol{c}}_i\times(\boldsymbol{x}_k-\boldsymbol{r}),$$
$$\hat{\boldsymbol{c}}_i := \frac{\boldsymbol{c}_i}{\|\boldsymbol{c}_i\|} \tag{23}$$

where $\mathbb{B}$ is the set of all discrete velocities at a boundary node $\boldsymbol{x}_k$, which intersect with the boundary, $\partial\Omega$ is the set of all boundary nodes around a particle of volume Ω, and $\boldsymbol{r}$ is the center of the mass. With $\boldsymbol{F}$ and $\boldsymbol{T}$ available, the particle

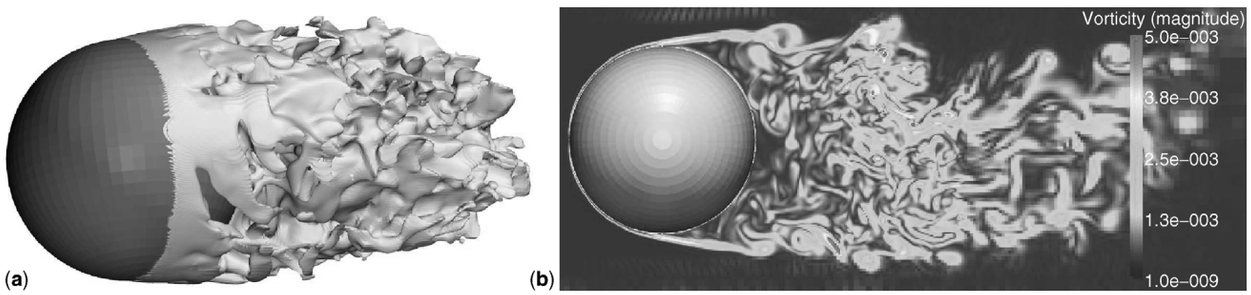

Figure 3. LBE-LES for the flow past a sphere at $Re = 10\,000$. (a) Instantaneous iso-surface of u_x in 3D and (b) $\|\boldsymbol{\omega}\|$ on the symmetric xy plane. Courtesy of S. Freudiger.

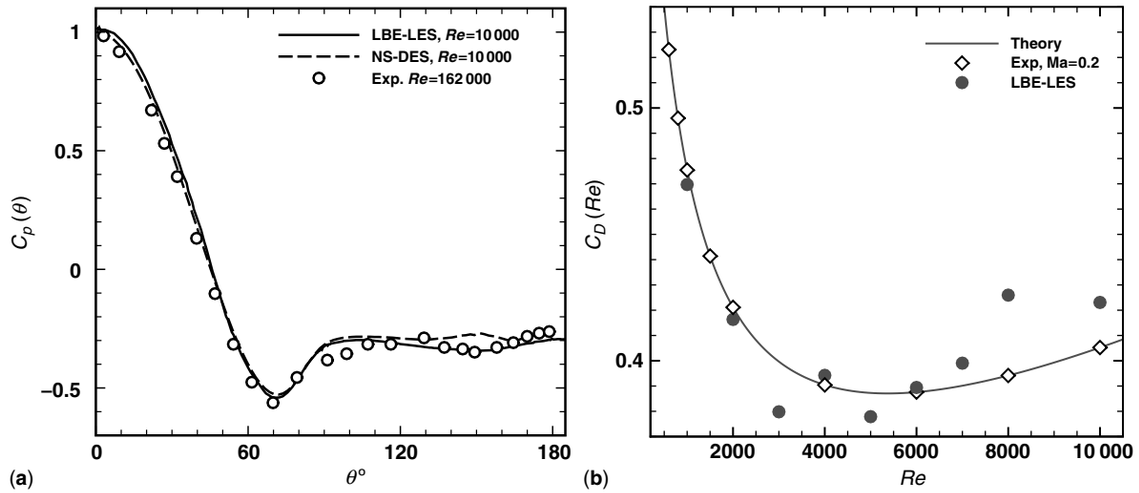

Figure 4. Flow past a sphere. (a) $\bar{C}_p(\theta)$ at $Re = 10\,000$, $\theta = 0^\circ$ is the stagnation point. (b) $C_D(Re)$, $1000 \leq Re \leq 10\,000$.

evolves according to Newton's law, and fluid–particle interactions are realized through no-slip boundary conditions (Ladd, 1994a, 1994b). For a system of multiple particles, a lubrication force must be considered to prevent overlaps of particles (Nguyen and Ladd, 2002).

Figure 5 shows the settling of a spherical cluster consisting of 1812 spheres under gravity. The cluster remains coherent for a surprisingly long period of time. At low Reynolds number the cluster remains spherical in shape, slowly shedding a trail of particles behind it. With a small amount of inertia, the particles redistribute and the cluster becomes a torus, which is a highly coherent state and no particles are lost from it. However, the radius of the torus eventually grows so large that it becomes unstable. It then breaks up into smaller clusters, which also take on a toroidal shape. The image on the far right of Figure 5 shows the late-stage fragmentation of the cluster into several daughter rings.

There is a striking similarity between the structures observed in the LB simulations and experimental results of Nicolas (2002), in particular the bending of the ring just prior to the break up into smaller clusters (cf. Figure 7 in Nicolas' paper). The fourth image in Figure 5 shows the bending of the torus prior to breakup.

2.4 A droplet sliding on an inclined surface

A two-component D3Q19 MRT-LBE model is used to simulate a droplet sliding down a 45° inclined surface under gravity. Two immiscible fluids "A" and "B" with $\rho_A : \rho_B = 1 : 10$ and $\nu_A : \nu_B = 100 : 1$ present ambient gas and the liquid droplet, corresponding to $\phi = +1$ and -1, respectively. The LB model has two parts: the velocity field $\boldsymbol{u}$ of the mixture is solved by using an LB Navier–Stokes solver, while the density fields of two individual fluids in the mixture, $\rho_A(\boldsymbol{x})$ and $\rho_B(\boldsymbol{x})$, are driven by $\boldsymbol{u}$ (Ahrenholz *et al.*, 2008). The mesh size is $60 \times 40 \times 60$, and the droplet radius is about $15\delta_x$. Periodic boundary conditions are applied in both x and y directions; the solid surface is at the bottom and free slip boundary conditions are applied at the top. The surface property can

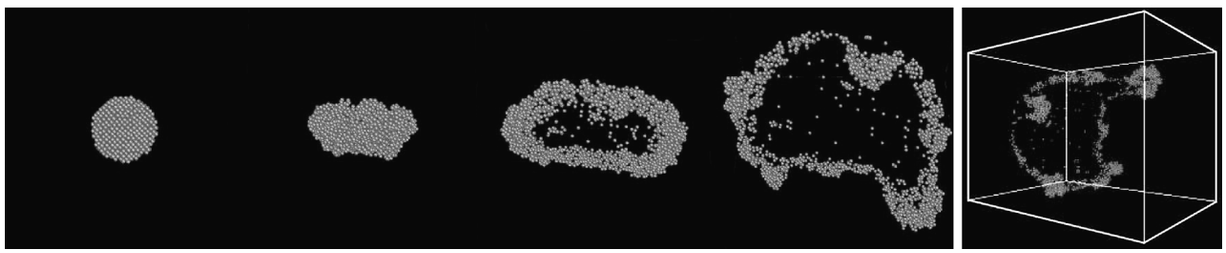

Figure 5. Settling of a spherical cluster of 1812 spheres under gravity. The mesh size is $400 \times 400 \times 1300$, the particle radius $R \approx 2.7\delta_x$, the particle Reynold number $Re \approx 0.3$, and the initial cluster about $80\delta_x$ in diameter. Time increases from left to right. The first four left figures are views from bottom, and the far right one is a side view. Courtesy of A.J.C. Ladd.

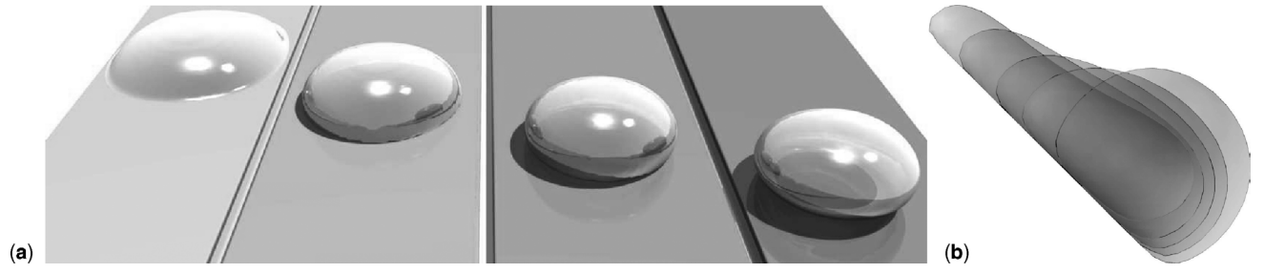

Figure 6. Droplets sliding down a 45° inclined surface under gravity. (a) Left to right, $\phi_w = -0.5$, 0.0, 0.5, and 1.0; (b) the final profiles of the droplet; as a reference, a symmetric droplet on a leveled surface with $\phi_w = 1.0$ is also shown. Courtesy of B. Ahrenholz.

be either hydrophilic ($\phi_w < 0$) or hydrophobic ($\phi_w > 0$) to the droplet. In the final state with a constant sliding velocity depending on gravity, the droplet attains different receding and preceding contact angles depending on the surface property specified by ϕ_w. Figure 6 shows the final states of droplets on the surfaces with different wettability. The numerical results of the contact angles agree well with theoretical predictions.

2.5 Flow through porous media

Figure 7 shows simulations of the residual air saturation after a liquid imbibition in natural soil samples (Tölke *et al.*, 2002; Tölke, Freudiger and Krafczyk, 2006; Ahrenholz *et al.*, 2008). A mesh of size 200^3 is used to resolve the samples, which are digitized by CT scan techniques. The grid size is $\delta_x \approx 11\,\mu$m. The simulations can be used to determine the sensitivity of the computed transport coefficients for unsaturated soil on porosity ϕ and the representative elementary volume necessary to derive the macroscopic transport properties.

3 CONCLUSIONS AND OUTLOOK

In this article we provide a concise survey of the lattice Boltzmann equation: its mathematical theory and its capabilities for CFD applications. Due to the space limitation, we do not discuss the LB applications for thermo-hydrodynamics, non-Newtonian fluids, and micro-flows with non-zero Knudsen number effects. A more extensive review has been given by Yu *et al.* (2003). Although the LBE is still in its infancy, it has shown great potential in a number of areas,

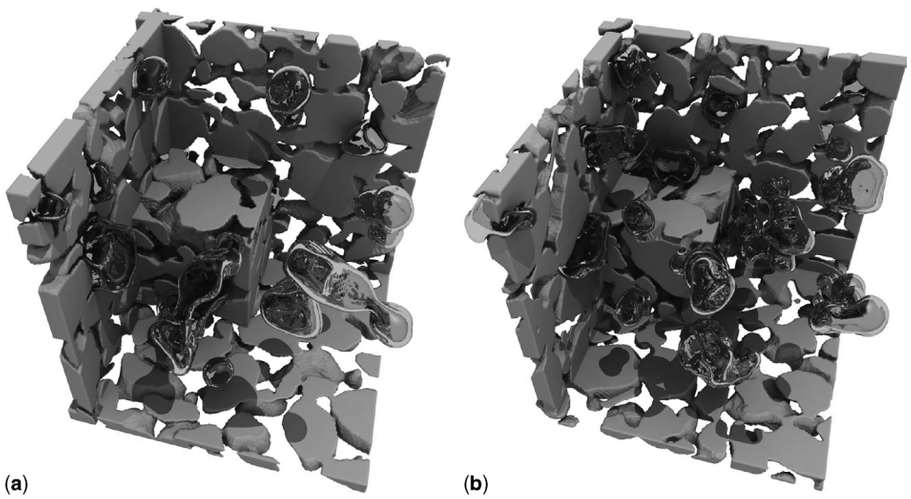

Figure 7. Immiscible fluids through porous media. Residual air saturation after liquid imbibition. Only the residual air is shown. (a) The porosity $\phi = 0.412$; (b) 0.388. Courtesy of B. Ahrenholz.

as demonstrated by the examples shown in this survey. The LBE has two noteworthy advantages. The first is numerical. We note that the Boltzmann equation (1) is a first-order *linear* equation with a linear advection term $\boldsymbol{\xi}\cdot\nabla f = \nabla\cdot(\boldsymbol{\xi} f)$ and a nonlinear but *local* collision term. The first-order system is easier to handle numerically. The second advantage is physical. Due to its kinetic origin, the LBE has the potential to model extended hydrodynamics, which is beyond the validity of the Navier–Stokes–Fourier theory.

The lattice Boltzmann method is an explicit second-order method and has yet to employ many sophisticated numerical techniques that have been well developed for CFD applications. Although there are some preliminary studies of using implicit time stepping, multigrid, and higher-order discretizations in the LBE, to develop LB algorithms with these sophisticated techniques will remain the areas of active research in the foreseeable future.

ACKNOWLEDGMENTS

The authors are grateful to Prof. A.J.C. Ladd for providing the materials related the LB simulation of particulate suspension shown in Figure 5, Prof. G. Constantinescu for the DES data shown in Figure 4, Dr. S. Freudiger for Figures 3 and 4 from his PhD thesis, and Dr. B. Ahrenholz for Figures 6 and 7 from his PhD thesis. LSL would like to thank Dr. J. Tölke for helpful discussions. LSL would also like to acknowledge the support from the US National Science Foundation for this work under Grant No. DMS-0807983. MK would like to acknowledge the support from DFG and BMBF.

REFERENCES

Ahrenholz, B., Tölke, J., Lehmann, P., Peters, A., Kaestner, A., Krafczyk, M. and Durner, W. (2008) Prediction of capillary hysteresis in a porous material using lattice-Boltzmann methods and comparison to experimental data and a morphological pore network model. *Adv. Water Res.*, **31**(9), 1151–1173.

Achenbach, E. (1972) Experiments on the flow past spheres at very high Reynolds numbers. *J. Fluid Mech.*, **54**(3), 565–575.

Asinari, P. and Luo, L.-S. (2008) A consistent lattice Boltzmann equation with baroclinic coupling for mixture. *J. Comput. Phys.*, **227**(8), 3878–3895.

Bouzidi, M., Firdaouss, M. and Lallemand, P. (2001) Momentum transfer of Boltzmann-lattice fluid with boundaries. *Phys. Fluids*, **13**(11), 3452–3459.

Chen, S. and Doolen, G. D. (1998) Lattice Boltzmann method for fluid flows. *Annu. Rev. Fluid Mech.*, **30**, 329–364.

Clift, R., Grace, J.R. and Weber, M.E. (1978) *Bubbles, Drops and Particles*, Academic Press, New York, p. 112.

Constantinescu, G. and Squires, K. (2004) Numerical investigations of flow over a sphere in the subcritical and supercritical regimes. *Phys. Fluids*, **16**(5), 1449–1466.

d'Humières, D. (1992) Generalized lattice-Boltzmann equations, in *Rarefied Gas Dynamics: Theory and Simulations* (eds B.D. Shizgal and D.P. Weave), vol. 159, *Progress in Astronautics and Aeronautics*, AIAA, Washington, D.C. pp. 450–458.

d'Humières, D., Ginzburg, I., Krafczyk, M., Lallemand, P. and Luo, L.-S. (2002) Multiple-relaxation-time lattice Boltzmann models in three-dimensions. *Philos. Trans. R. Soc. Lond. A*, **360**(1792), 437–451.

Ginzburg, I. and d'Humières, D. (2003). Multireflection boundary conditions for lattice Boltzmann models. *Phys. Rev. E*, **68**(6), 066614.

Goin, K.L. and Lawrence, W.R. (1968) Subsonic drag of spheres at Reynolds numbers from 200 to 10 000. *AIAA J.*, **6**(5), 961–962.

He, X. and Luo, L.-S. (1997). Theory of lattice Boltzmann method: From the Boltzmann equation to the lattice Boltzmann equation. *Phys. Rev. E*, **56**(6), 6811–6817.

Junk, M., Klar, A. and Luo, L.-S. (2005) Asymptotic analysis of the lattice Boltzmann equation. *J. Comput. Phys.*, **210**(2), 676–704.

Krafczyk, M., Tölke, J. and Luo, L.-S. (2003) Large-eddy simulations with a multiple-relaxation-time LBE model. *Int. J. Mod. Phys. B*, **17**(1/2), 33–39.

Ladd, A.J.C. (1994a) Numerical simulations of particulate suspensions via a discretized Boltzmann equation. Part 1. Theoretical foundation. *J. Fluid Mech.*, **271**, 285–309.

Ladd, A.J.C. (1994b). Numerical simulations of particulate suspensions via a discretized Boltzmann equation. Part 2. Numerical results. *J. Fluid Mech.*, **271**, 311–339.

Lallemand, P. and Luo, L.-S. (2000) Theory of the lattice Boltzmann method: Dispersion, dissipation, isotropy, Galilean invariance, and stability. *Phys. Rev. E*, **61**(6), 6546–6562.

Lallemand, P. and Luo, L.-S. (2003) Theory of the lattice Boltzmann method: Acoustic and thermal properties in two and three dimensions. *Phys. Rev. E*, **68**(3), 036706.

Luo, L.-S. (2000) Theory of lattice Boltzmann method: Lattice Boltzmann models for nonideal gases. *Phys. Rev. E*, **62**(4), 4982–4996.

Maríe, S., Ricot, D. and Sagaut, P. (2009) Comparison between lattice Boltzmann method and Navier–Stokes high-order schemes for computational aeroacoustics. *J. Comput. Phys.*, **228**(4), 1056–1070.

Nicolas, M. (2002) Experimental study of gravity-driven dense suspension jets. *Phys. Fluids*, **14**(10), 3570–3576.

Nguyen, N.-Q. and Ladd, A.J.C. (2002) Lubrication corrections for lattice-Boltzmann simulations of particle suspensions. *Phys. Rev. E*, **66**(4), 046708.

Peng, Y., Liao, W., Luo, L.-S. and Wang, L.-P. (2009) Comparison of the Lattice Boltzmann and Pseudo-Spectral Methods for Decaying Turbulence: Low Order Statistics. To appear in *Comput. Fluids*.

Rothman, D.H. and Zaleski, S. (1997) *Lattice-Gas Cellular Automata: Simple Models of Complex Hydrodynamics*. Cambridge University Press, Cambridge, UK.

Tölke, J., Freudiger, S. and Krafczyk, M. (2006) An adaptive scheme using hierarchical grids for lattice Boltzmann multi-phase flow simulations. *Comput. Fluids*, **35**(8/9), 820–830.

Tölke, J., Krafczyk, M., Schulz, M. and Rank, E. (2002) Lattice Boltzmann simulations of binary fluid flow through porous media. *Philos. Trans. R. Soc. Lond. A*, **360**(1792), 535–545.

Yu, D., Mei, R., Luo, L.-S. and Shyy, W. (2003) Viscous flow computations with the method of lattice Boltzmann equation. *Prog. Aerospace Sci.*, **39**(5), 329–367.

Yu, H., Luo, L.-S. and Girimaji, S.S. (2006) LES of turbulent square jet flow using an MRT lattice Boltzmann model. *Comput. Fluids*, **35**(8/9), 957–965.